RESEARCH PAPER

Convection–diffusion molecular transport in a microfluidic bilayer device with a porous membrane

Timothy S. Frost[1] · Victor Estrada[2] · Linan Jiang[2] · Yitshak Zohar[1,2]

Abstract

The field of human cell research is rapidly changing due to the introduction of microphysiological systems, which commonly feature two stacked microchannels separated by a porous membrane for in vitro barrier modeling. An essential component to adequately representing a subset of human organ or tissue functions in these microfluidic systems is the concentration distribution of the biospecies involved. In particular, when different cell types are cultured, a delicate balance between media mixing and cellular signaling is required for long-term maintenance of the cellular co-culture. In this work, we experimentally measured the effects of various control parameters on the transient and steady average molecular concentration at the bilayer device outlet. Using these experimental results for validation, we then numerically investigated the concentration distributions due to the convection–diffusion mass transport in both microchannels. The effects of media flow rate, separation membrane porosity, molecular size, microchannel dimensions and flow direction have been systematically characterized. The transient response is found to be negligible for cell co-cultures lasting several days, while the steady-state concentration distribution is dominated by the media flow rate and separation membrane porosity. Numerically computed concentration profiles reveal self-similarity characteristics featuring a diffusive boundary layer, which can be manipulated for successful maintenance of cell co-culture with limited media mixing and enhanced cell signaling.

Keywords Microfluidic bilayer device · Convection–diffusion mass transport · Molecular concentration distribution

1 Introduction

Bio-microfluidic research is rapidly growing into a multi-billion dollar industry with an expansive array of applications among bio-tech companies (Volpatti and Yetisen 2014; Zhang and Radisic 2017). One of the most attractive bio-microfluidic applications are microphysiological systems (MPSs), which are in vitro models that capture important aspects of in vivo organ function through the use of specialized culture microenvironments (Edington et al. 2018). These microfluidic systems, often termed organs-on-chips (OoCs), incorporate small, plastic devices. The devices are designed to enable modeling certain human organs and trigger more accurate cellular responses compared to their static 2D culture counterparts (Huh et al. 2010, 2012). MPS technology has begun to accelerate medical research across several fields. In drug discovery, these models are being implemented by major companies to perform high-throughput assays to assess drug viability, optimizing clinical trials, and potentially reducing R&D costs to develop new compounds (Marx et al. 2012). MPSs are also used for modeling of diseases, such as cancer, which is emerging as a prominent application driving development of complex systems with higher-order tissue functions (Edington et al. 2018).

MPSs offer several major advantages over traditional 2D or other 3D culture methods. Using microfluidic cell cultures grants the ability to precisely control concentration distributions to trigger certain cell responses (Siyan et al. 2009; Chung and Choo 2010). The resulting concentration gradients can induce chemotaxis, metabolic changes, wound healing, and even metastasis (Even-Ram and Yamada 2005; Zaman et al. 2005; Kinsey et al. 2011; Riahi et al. 2014). As research regarding MPSs progresses, it will be important to control the concentration gradients at physiologically

✉ Timothy S. Frost
  tfrost@email.arizona.edu

[1] Department Biomedical Engineering, University of Arizona, Tucson, USA

[2] Department Aerospace and Mechanical Engineering, University of Arizona, Tucson, USA

relevant levels to improve the representation of the human tissue (Wikswo et al. 2013). Additionally, MPSs allow the exposure of the modeled human tissue to experience flow-induced shear stress during culture. Shear stress has been known to be an integral and important part of the cellular environment (Merchuk 1991; Lipowsky 1995; Metallo et al. 2008).

Transwell inserts have been used to conduct permeability studies for barrier organs such as the intestine or lung (Winton et al. 1998; Hubatsch et al. 2007). The concentration distribution for these culture inserts has been well characterized, but the concentration distribution in MPSs is very different due to fluid flow. The balance between mass transport by convection and diffusion results in a concentration distribution specific to the MPS design (Glover et al. 2014).

Microfluidic devices have been established as the most common platforms to realize MPSs. However, challenges associated with controlling concentration levels and gradients persist. A typical microfluidic device comprising a cellular bilayer culture under fluid flow must handle tradeoffs between sustaining cell signaling and limiting media mixing. An analytical model was presented characterizing a microfluidic device, in which soluble factors are delivered to a cell population by means of flow through a proximate channel separated from the culture channel by a membrane (Inamdar et al. 2011). A detailed theoretical model of capillary transport in rectangular microchannels was proposed (Waghmare and Mitra 2012). Another theoretical study was carried out to evaluate the oxygen profile within a multilayer microfluidic device consisting of a gas reservoir, a PDMS membrane and a fluid channel with a cell culture layer (Kim et al. 2013). A mathematical model was developed to describe the transient convection, diffusion, dispersion and binding of ligands to surface receptors of cells cultured in a microchannel (Ramji and Roy 2013). A microfluidic device was proposed to rapidly generate various concentration gradients in a controllable manner for a chemotaxis study of motile bacterial cells (Kim et al. 2014). Another microfluidic device was introduced to monitor cell mechanical deformation after chemical cues are delivered to the cells via diffusion through a porous membrane (Ravetto et al. 2016).

Modeling of barrier–tissue interfaces in vitro has extensively been reviewed with a focus on the use of complex microfluidic platforms (Sakolish et al. 2016). A microfluidic chip comprising two parallel microchannels was developed for analyzing vascular and extravascular mass transport, over multiple spatial and temporal scales, in a variety of diseases (Manneschi et al. 2016). A drug combination screening microfluidic platform was reported enabling optimum concentration distribution (Sun et al. 2017). The convection–diffusion equation was solved analytically to investigate the spatio-temporal biochemical signals in pulsatile flows through microchannels (Li et al. 2018).

Although microfluidic bilayer devices with porous membranes have frequently been utilized, a comprehensive study of the effect of various control parameters on the resulting concentration distribution of a given biochemical species has yet to be published. Therefore, we present here a systematic study of the effects of the dominant control parameters on the convection–diffusion mass transport balance and the resulting molecular concentration distributions of a passive scalar contaminant. The experimental and numerical investigations were carried out in devices featuring basic elements common to MPSs used for modeling various barrier organs in the human body (Jang and Suh 2010; Huh et al. 2012; Kimura et al. 2018). The results have direct implications providing guidelines for designing devices for applications such as MPSs.

2 Methods

2.1 Experimental

2.1.1 Device design and fabrication

Microfluidic devices are designed to allow long-term co-cultures of different cell types for applications such as organs-on-chips. Each device features two microchannels stacked on top of each other and separated by a thin porous membrane. The microchannels were formed by dispensing a thin layer of polydimethylsiloxane (PDMS) polymer solution on a pre-fabricated relief mold. An aluminum mold was used for deep 450-μm-high channels, and a silicon mold was used for shallow 120-μm-high channels. Upon curing at 55 °C for 24 h, the PDMS substrate was peeled off the mold with grooves, each was about 1 mm wide and 35 mm long. A 15 G blunt needle was used to punch holes for inlets and outlets in each microchannel. Pairs of microchannels were aligned, overlapping only along the middle 20 mm sections, and bonded together with a porous polyester membrane sandwiched between them. Prior to bonding, the surfaces of the PDMS substrates and separation membrane were treated for enhanced adhesion to prevent leakage during long-term operation. The PDMS substrates were plasma treated for 1 min (Harrick Plasma, 30 W, 1000 mTorr) to render their surfaces hydrophilic. The track-etched membrane was also plasma treated for 1 min and soaked for 30 min at 55 °C in a 5% (v/v) solution of (3-Aminopropyl) triethoxysilane (APTES) in water for leakage-free sealing (Song et al. 2018). The membrane was dried and layered between the plasma-treated PDMS surfaces for final assembly. Once firm bonding had been achieved, tubing adapters were placed over the punched holes to serve as inlet/outlet connectors to the external fluid handling system. An image of a fabricated and packaged microfluidic device, filled with
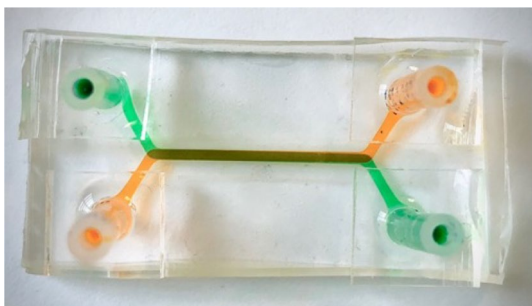
Fig. 1 An image of a fabricated microfluidic device; the top channel (orange) and bottom channel (green) are stacked vertically with a porous separation membrane sandwiched between them (color figure online)
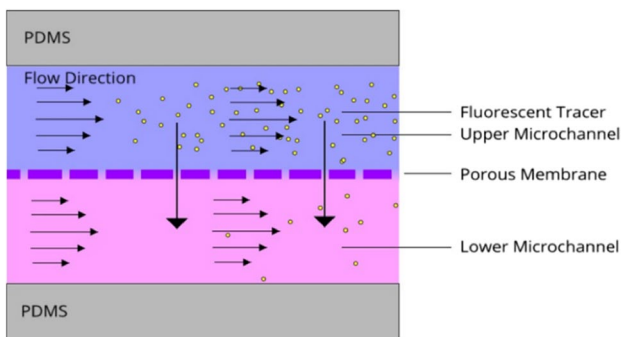

Fig. 2 A schematic of the convection/diffusion mass transport balance in the microfluidic device; molecules from the high-concentration stream (purple) diffuse into the low-concentration stream (pink) while convected downstream (color figure online)

colored liquids, is shown in Fig. 1. Each microchannel has a dedicated inlet and outlet to independently control both the fluid content and flow rate.

2.1.2 Setups and measurements

Experiments were conducted by driving a solution of fluorescently labeled molecules at a pre-determined concentration through the top channel under constant flow rate, while driving only water at the same flow rate through the bottom channel as illustrated in Fig. 2. Both flow rates were controlled using a syringe pump. Since the flow rate and dimensions of both microchannels are the same in all experiments, the pressure difference across the porous separation membrane is zero. Consequently, under such conditions, molecular transfer between the two channels is governed by diffusion due to the concentration gradient across the membrane which, in turn, depends on the velocity field.

Two different setups were used to investigate the time-dependent and steady-state behavior of the microfluidic system. For the transient response study, a fluorescent microscope equipped with a CCD camera was used to record the light intensity level at the bottom channel outlet every 5 min. For the steady-state study, 500 µL samples of each channel outlet flow were collected and separated into 100 µL aliquots on a 96-well plate. The fluorescence intensity level of the samples was recorded using a Biotek Synergy two plate reader, and the average intensity among the five aliquots was taken as the steady-state value. The deviations from the average value were used to estimate the experimental error.

A calibration curve has been established for each fluorescently labeled molecule used in the experiments to relate the light intensity raw data to molecular concentration values. The curves are roughly linear at low concentration but highly nonlinear at high concentration. To avoid the saturation range, where the light intensity changes very little if at all with changes in concentration, the experiments were designed to ensure that all measured data were within the linear range. In both setups, the average light intensity at a channel outlet is measured, while the molecular concentration in each microchannel is a function of space and time, $c(x, y, z; t)$. Therefore, using the calibration curve, the converted value is the temporal average concentration at the channel outlet $C(t)$ defined as:

$$C(t) = \left[\int_{-W/2}^{W/2} \int_{-H}^{0} c(x = L/2, y, z; t) \mathrm{d}y \mathrm{d}z \right] \Big/ (WH), \quad (1)$$

where H, W, and L are the channel height, width and length, respectively, and at steady state $C_\infty = C(t \to \infty)$. The origin of the coordinate system is the center of the device such that the fluid domain is confined to: $-L/2 \leq x \leq L/2$, $-H \leq y \leq H$, and $-W/2 \leq z \leq W/2$.

Repeatability of concentration measurements, especially based on light intensity records, is known to be notoriously challenging due to a myriad of sources. Uncertainties in experimental variables such as, microchannel dimensions, initial solution concentration, flow rate, sample volume, membrane porosity, light intensity level and its conversion to molecular concentration all contribute to a large experimental error. To reliably estimate the error for each data point, the same experiment would have to be repeated enough times to allow a meaningful statistical analysis. However, this approach is not practical here since it requires an enormous number of experiments to evaluate the effects of several parameters of interest detailed in the next section. In an alternative approach, therefore, experiments have been repeated several times only for a small set of combinations and analyzed based on the error with respect to the average concentration of each set, $\bar{C}$. Some 400 individual trials, using the same setup but different experimental parameters are compiled in the histogram
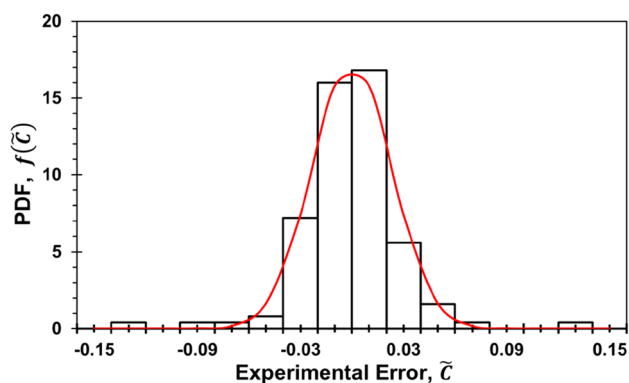
Fig. 3 A histogram of scaled experimental error in concentration measurements fitted with a normal probability distribution function (red solid curve) (color figure online)

shown in Fig. 3. The histogram is normalized and fitted with the following normal probability distribution function (PDF), $f(\tilde{C})$:

$$f(\tilde{C}) = \frac{1}{\sqrt{2\pi\sigma^2}} e^{-\frac{\tilde{c}^2}{2\sigma^2}} \quad \text{where} \quad \tilde{C} = \frac{C - \bar{C}}{C_0}, \qquad (2)$$

such that the integral of the PDF is equal to unity; C_0 is the initial concentration at the top channel inlet. The PDF standard deviation, $\sigma = 0.03$, is taken as the estimated experimental error.

2.1.3 Operational conditions

The effects of several parameters on the transient and steady-state molecular concentration distributions in microchannel pairs, due to the convection–diffusion flow field, have been systematically studied experimentally and numerically. Apart from the flow rate, which directly impacts convection, other tested parameters include: membrane porosity, molecular size/diffusivity, channel height, and flow direction. In each experiment, for both co-current and counter-current modes, the flow rates in both microchannels were equal and constant in time. A syringe pump was used to adjust the flow rate in the range of 20–200 μL/h. Experiments with flow rates below 20 μL/h proved difficult to repeat as the minute pressure drop generated by the syringe pump was countered by any device irregularity yielding unreliable data. For flow rates higher than 200 μL/h, diffusion is negligible resulting in undetectable molecular transport across the separation membrane between the two channels.

Three commercially available polyester membranes (it4ip, Belgium), about 23 μm in thickness, were tested to explore the membrane porosity effect with pore size of 0.4 μm, 0.8 μm, and 3 μm with 0.3%, 1%, and 10% porosity, respectively; the porosity is defined as the ratio between the total pore area and total membrane area. Both the pore diameter and pore density were measured using SEM images to confirm the technical specifications provided by the manufacturer. The selected porosity range represents typical membranes used in fabricating devices for cell culture applications such as organs-on-chips (Jang and Suh 2010; Huh et al. 2012; Esch et al. 2012).

To study the molecular-size effect, three types of fluorescently labeled molecules were used in the experiments varying in size and diffusivity as follows: fluorescein (0.332 kDa, 5.4×10^{-10} m²/s), (Riahi et al. 2014) Lucifer yellow (0.457 kDa, 5.0×10^{-10} m²/s) (Heyman and Burt 2008) and dextran (70 kDa, 5.6×10^{-11} m²/s) (Jain 1984). These molecules are widely available and commonly used in permeability studies (Foster et al. 1998; Salomon et al. 2014). Based on the calibration curves, initial concentrations of $C_0 = 1$, 7 and 100 μM were selected for dextran, fluorescein and Lucifer yellow, respectively.

The microchannel height effect was evaluated by utilizing microfluidic devices with microchannels either 120 μm or 450 μm in height. The microchannel height was measured directly from its cross-section. Together with the designed channel width and length, these are typical dimensions of organs-on-chips devices employed for barrier permeability studies (Sellgren et al. 2014; Ruiz et al. 2014; Rotenberg et al. 2012).

Lastly, the effect of flow direction was observed by reversing the flow direction in one microchannel, in the counter-current mode, in comparison with the co-current mode where both flows were in the same direction. The concept of manipulating molecular transport by controlling the flow direction stems from heat exchanger designs where heat transfer in counter-current flows can exceed the theoretical limit for heat transfer in co-current flows (Dichamp et al. 2017).

2.2 Numerical

2.2.1 Theoretical modeling

The spatio-temporal molecular concentration distribution in each microchannel, $c(x, y, z; t)$, is a result of the balance between two mass transport mechanisms: convection and diffusion. Since only liquid flows are considered, the convection is modeled using the incompressible Navier–Stokes equation:

$$\rho\left[\frac{\partial \mathbf{u}}{\partial t} + \mathbf{u} \cdot \nabla \mathbf{u}\right] = -\nabla P + \mu\Delta \mathbf{u} + \rho\mathbf{g}. \qquad (3)$$

Here, ρ is the fluid density, $\mathbf{u}$ is the velocity vector field, t is time, P is the pressure, μ is the fluid viscosity, and $\mathbf{g}$ represents the gravity vector. The concentration distribution

of a given species is then governed by the convection–diffusion equation:

$$\frac{\partial C}{\partial t} + \mathbf{u} \cdot \nabla c = D \nabla^2 c, \tag{4}$$

where D is the diffusion coefficient of the species of interest. The no-slip boundary condition is imposed on both channel and membrane surfaces. In all experiments, the initial concentration at the top channel inlet is uniform and finite, $c(x/L = -0.5, 0 \leq y/H \leq 1, -0.5 \leq z/W \leq 0.5; t = 0) = C_0$, while the initial concentration at the bottom channel inlet is zero, $c(x/L = -0.5, -1 \leq y/H \leq 0, -0.5 \leq z/W \leq 0.5; t = 0) = 0$.

2.2.2 Numerical simulations

The numerical simulations were performed using ANSYS Fluent. The separation membrane has been modeled by setting the velocity to zero at its location, and the porosity was modeled by scaling the molecular diffusivity by the void area created by the membrane pores (Pisani 2011). The molecular diffusion coefficients were estimated based on the Stokes–Einstein equation:

$$D = \frac{k_B \cdot T}{6 \pi \mu r} \quad \text{with} \quad r = \left(\frac{3M}{4\pi N} \right)^{1/3}, \tag{5}$$

where k_B is the Boltzmann constant, T is the temperature, and r is a radius calculated based on the molecular weight, M, and the Avogadro number, N (Erickson 2009; Ravetto et al. 2016). A Green–Gauss node-based solver was used to minimize artificial diffusion.

3 Results and discussion

Transient and steady-state concentration distributions in microfluidic devices have been investigated experimentally and numerically under various initial conditions. The numerical code is validated via a direct comparison between computed and available measured values, and it has been extended to compute concentration distributions for which no experimental measurements are available.

3.1 Microfluidic device transient response characterization

The time-dependent response of the microfluidic device, which is important in many permeability studies, is characterized. The initial condition for the temporal experiments includes a solution with uniform molecular concentration distribution, C_0, at rest in one microchannel and pure water with zero molecular concentration at rest in the other microchannel. At $t = 0$, the pump is triggered to drive the

two liquids under the same constant flow rate, Q, along the two microchannels. As the molecules are transported downstream by convection, they are simultaneously transported from one microchannel to the other through the separation membrane due to concentration gradients. Consequently, the molecular concentration at the water channel output increases with time from zero to a steady-state concentration. Both the time needed to reach a steady state and the steady-state concentration level depend on the experimental conditions. The effects of various operational conditions on the microfluidic system transient response were investigated by measuring the bulk molecular concentration at the water channel outlet as a function of time. The results are summarized in Fig. 4, where each data set is fitted by an exponential curve, $C/C_0 = A \cdot [1 - \exp(-t/B)]$, where A and B are fitting parameters.

The flow rate effect is explored first since it is the dominant parameter controlling the convective mass transport. The time-dependent relative concentrations of fluorescein are plotted in Fig. 4a for $Q = 20$, 50 and 100 µL/h with 1%
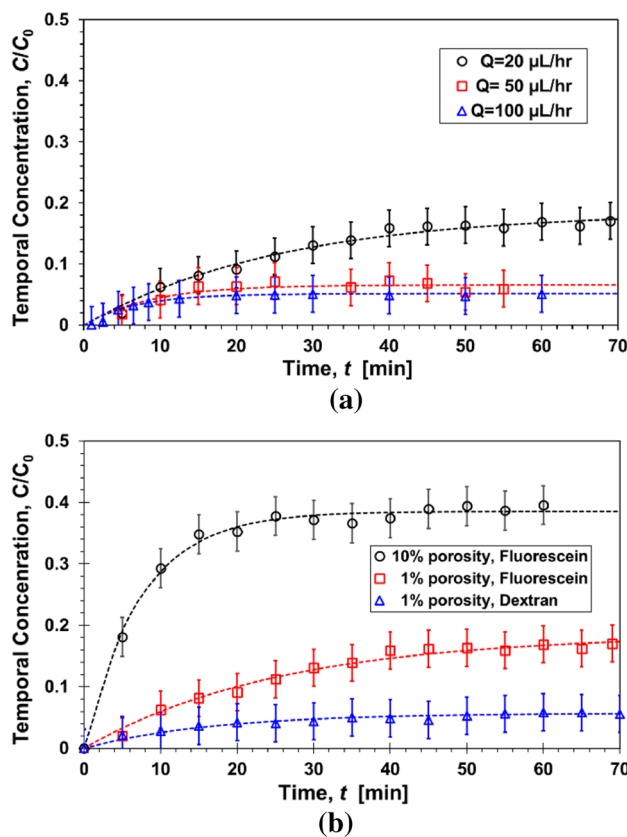

Fig. 4 Time-dependent concentration measurements (symbols) and computations (dash lines) at the water channel outlet of: **a** fluorescein with 1% membrane porosity for different flow rates, and **b** fluorescein with membrane porosity of 1% and 10% as well as dextran with 1% porosity to highlight the effect of membrane porosity and molecular size under parallel liquid flows at a constant rate of 20 µL/h

membrane porosity in 450-µm-high microchannels. Both the steady-state level and time to reach steady state increase with decreasing flow rate. The effects of other variables, such as membrane porosity and molecular size, on the system transient response have also been investigated. Temporal concentration measurements of fluorescein with 1% and 10% membrane porosity as well as measured concentrations of dextran with 1% porosity, under a constant flow rate of 20 µL/h, are plotted in Fig. 4b. Increasing the diffusion area by an order of magnitude, as the membrane porosity increases from 1 to 10%, increases the measured fluorescein concentration only by a factor of about 2.5. Similarly, decreasing the dextran diffusivity by one order of magnitude compared to the fluorescein diffusivity, with the same 1% membrane porosity, increases the molecular concentration just by a factor of about 3. These results underscore the highly nonlinear characteristics of the system.

The two parameters characterizing the measured temporal concentration curves are the steady-state concentration level at the bottom channel outlet, C_∞, and the time scale required for the system to reach steady state, T. It is straightforward to obtain the steady-state concentration from the collected data but not the time scale. The molecular transfer in the microfluidic device, due to convection and diffusion, clearly cannot be modeled as a first-order linear system. Nevertheless, as shown in Fig. 4, the close agreement between the measured data sets and the corresponding exponential curves provides a reliable estimate of both the steady-state concentration, $C_\infty/C_0 = A$, and the time scale, $T = B$, which is the time required to achieve 63.2% of the steady-state concentration level. Normalized time-dependent concentration curves, using C_∞ and T as scaling parameters, are plotted in Fig. 5a for a variety of experimental conditions. The reasonable collapse of multiple data sets onto a single curve indicates that, in spite of the microfluidic system complexity, these two parameters are sufficient to fairly characterize its transient behavior.

The two estimated parameters, C_∞/C_0 and T, used for scaling the flow rate-dependent data sets are graphed in Fig. 5b. The characteristic time scale for the tested flow-rate range is less than 1 h. In typical applications of such a microfluidic device, e.g., organs-on-chips, cells are cultured for several days and weeks. Hence, in such cell culture applications, the system is most likely at steady state during its entire operation; therefore, the transient phenomenon lasting for such a small fraction of time can be neglected altogether.

3.2 Steady-state molecular concentration distribution

The characteristic time scale for the microfluidic system response is found to be very short, less than 1 h, whereas this microfluidic device is typically designed for long-term
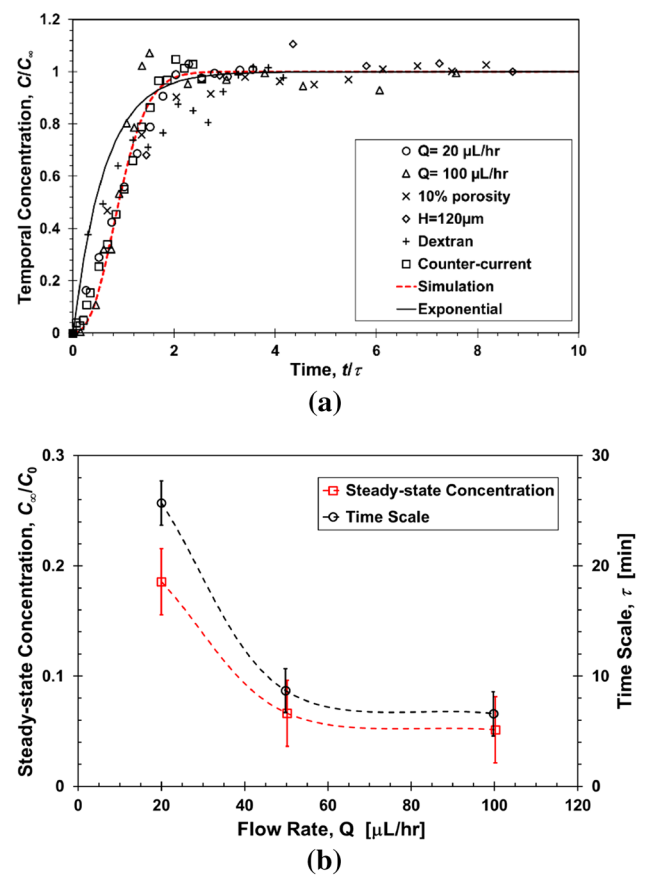

Fig. 5 a Scaled time-dependent molecular concentration measurements at the water channel outlet under various parameter combination (symbols) in comparison with numerical computations (dash line) and an exponential function (solid line), and **b** fitted scaling parameters, C_∞ and T, as a function of flow rate for fluorescein with 1% porosity

maintenance of cell cultures. Therefore, the steady-state molecular concentration distribution is the most relevant parameter in many applications. Since it is very difficult to experimentally measure cross-stream molecular concentration distributions, the steady-state molecular concentration measured at the channel outlet is utilized as a measure to investigate the effects of the following parameters: flow rate, membrane porosity, molecular size, microchannel height, and flow direction on the molecular transfer across the separation membrane between the microchannels.

3.2.1 Flow rate effect on molecular concentration

The flow rate is expected to be the most dominant parameter controlling the transfer of molecules across the separation membrane as it can be varied from no flow condition resulting in complete mixing of the two streams, i.e., $C_\infty = C_{T\infty} = C_0/2$, to a flow rate high enough to render cross-membrane diffusion negligible such that $C_\infty \to 0$
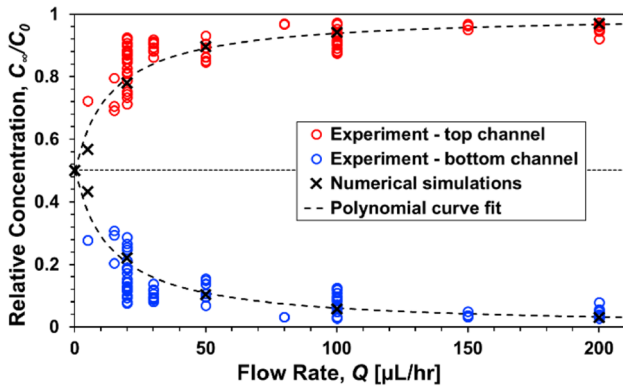
Fig. 6 Steady-state fluorescein concentration measurements and computations (symbols) at the top and bottom channel outlets as a function of the flow rate, fitted with a polynomial function (dash line), with 1% membrane porosity

and $C_{T\infty} \to C_0$; the subscript 'T' denotes top channel. Conservation of mass dictates that molecular gain in the bottom channel is equal to the loss in the top channel with the sum total being equal to the initial concentration, i.e., $(C_\infty + C_{T\infty})/C_0 = 1$. To quantify the flow rate effect, steady-state molecular concentration of fluorescein was measured at both outlets of 450-μm-high microchannels with 1% membrane porosity and co-current flows. The experimental measurements are compared with numerical computations in Fig. 6, and the results are fitted with a polynomial function. Some experiments were conducted multiple times to establish the repeatability and uncertainty involved in these concentration measurements, and the close agreement between the two sets of data validates the numerical simulations. As expected, the bottom channel outlet concentration decreases and the top channel outlet concentration increases with increasing flow rate. The sum of both relative concentrations, within experimental error, is indeed about unity. The best polynomial fit is obtained for $C_\infty/C_0 = 0.5a/(a + Q)$ with $a = 10$ and $C_{T\infty}/C_0 = 1 - C_\infty/C_0$ suggesting that the measured relative concentration in the bottom channel outlet is roughly inversely proportional to the flow rate, i.e., $C_\infty/C_0 \propto 1/Q$. Two flow regimes are apparent with $Q = 50$ μL/h as the transition flowrate. In the higher flow rate regime, $Q > 50$ μL/h, the diffusion mechanism is negligible compared to convection; as a result, both the relative steady-state concentration of about 5% and the time constant of less than 10 min change very little with increasing flow rate. In the lower flow rate regime, $Q < 50$ μL/h, the diffusion and convection mechanisms are comparable; consequently, both the steady-state value and time scale increase substantially with decreasing flow rate. Under a flow rate range used in cell culture applications, 10 μL/h < Q < 30 μL/h, there can be a significant degree of mixing across the membrane resulting in a relative concentration of 10–30% at the bottom channel outlet.

3.2.2 Membrane porosity and molecular-size effects

The effect of several other parameters on the steady molecular concentration at the bottom channel outlet has also been investigated. To demonstrate the membrane porosity effect, steady-state fluorescein concentration is plotted as a function of the flow rate for 0.3, 1 and 10% porosity, Fig. 7a, and as a function of the porosity for 20, 50, 100 and 200 μL/h flow rate, Fig. 7b. Under any finite flow rate, $Q > 0$, higher porosity membrane means larger mass transfer area resulting in higher steady-state concentration, which increases with decreasing flow rate. However, under static conditions ($Q = 0$) with non-zero porosity, complete mixing is expected resulting in $C_\infty/C_0 = 0.5$ independent of the membrane porosity. Mass transfer across the membrane is completely blocked with zero membrane porosity resulting in $C_\infty/C_0 = 0$ independent of the flow rate. As the membrane porosity approaches 100%, the steady-state concentration increases with decreasing flow rate. Interestingly, nearly complete mixing ($C_\infty/C_0 \approx 0.5$) can be achieved at only 30% porosity under a low flow rate of about 20 μL/h.
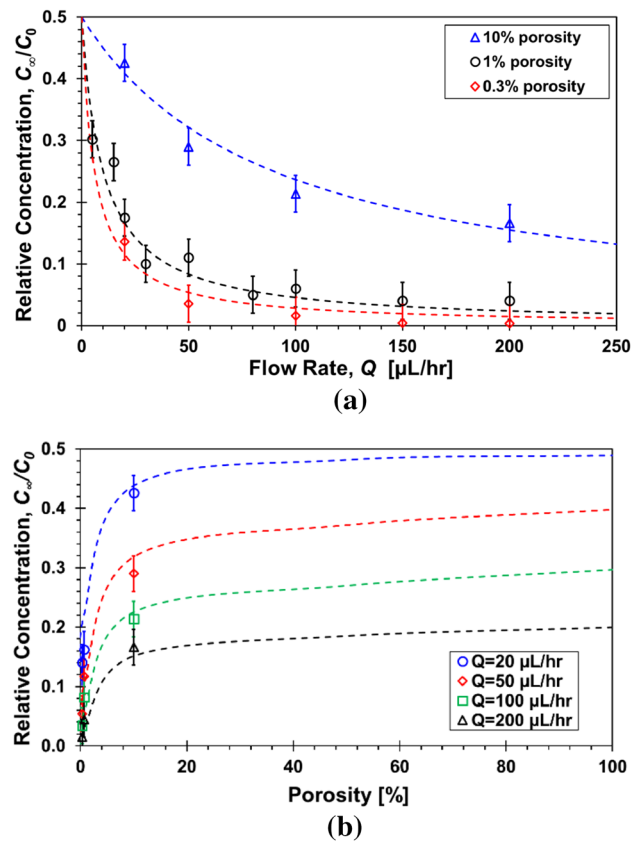

(a)

(b)

Fig. 7 Relative fluorescein concentration measurements (symbols) and computations (dash lines) at the bottom channel outlet as a function of: **a** flow rate for 0.3, 1, and 10% porosity, and **b** porosity for 20, 50, 100, and 200 μL/h flow rates

Mass flux is directly proportional to both concentration gradient and diffusion coefficient (Fick's first law). Hence, under the same experimental conditions, the concentration distribution in the microfluidic device will be different for molecules varying in diffusivity due to their size difference. To evaluate this effect, steady-state concentrations of small Lucifer yellow (0.457 kDa) and large dextran molecules (70 kDa) are plotted as a function of the flow rate, Fig. 8a, and as a function of the molecular diffusivity for 20, 50, 100 and 200 μL/h flow rate, Fig. 8b, with 1% porosity.

The steady-state concentration of Lucifer yellow with the higher diffusivity, $D = 5.0 \times 10^{-10}$ m^2/s, is consistently higher than that of dextran with the lower diffusivity, $D = 5.6 \times 10^{-11}$ m^2/s. Except for $Q = 0$ where the steady-state concentration of $C_\infty/C_0 = 0.5$ is independent of the diffusion coefficient, the difference between the steady-state concentrations depends on the flow rate. Increasing the diffusion coefficient by about one order of magnitude results in increased concentration by only a factor of about 2.5 under some flow rates. For large molecules with small diffusion coefficient, $D < 10^{-11}$ m^2/s, convection is dominant with

negligible diffusion resulting in vanishing concentration $C_\infty \to 0$, for any practical flow rate, $Q > 5$ μL/h.

3.2.3 Microchannel height and flow direction effects

The velocity and concentration distributions in each microchannel depend on its geometry. Since the molecular concentration distribution is expected to be roughly 2D, i.e., $\partial C/\partial z \approx 0$, the channel width should have a negligible effect compared to its height. Therefore, the effects of only the channel height and length have been studied. Steady-state fluorescein concentration at the water channel outlet is plotted as a function of the flow rate for devices with channel height of 120 and 450 μm, Fig. 9a, and as a function of the channel height for 20, 50, 100 and 200 μL/h flow rate, Fig. 9b, with 1% porosity.

As the channel height increases, under the same flow rate, the velocity near the membrane decreases. Reducing the convection contribution would enhance the molecular transfer rate across the membrane due to diffusion. On the other hand, for the same initial concentration, the cross-stream
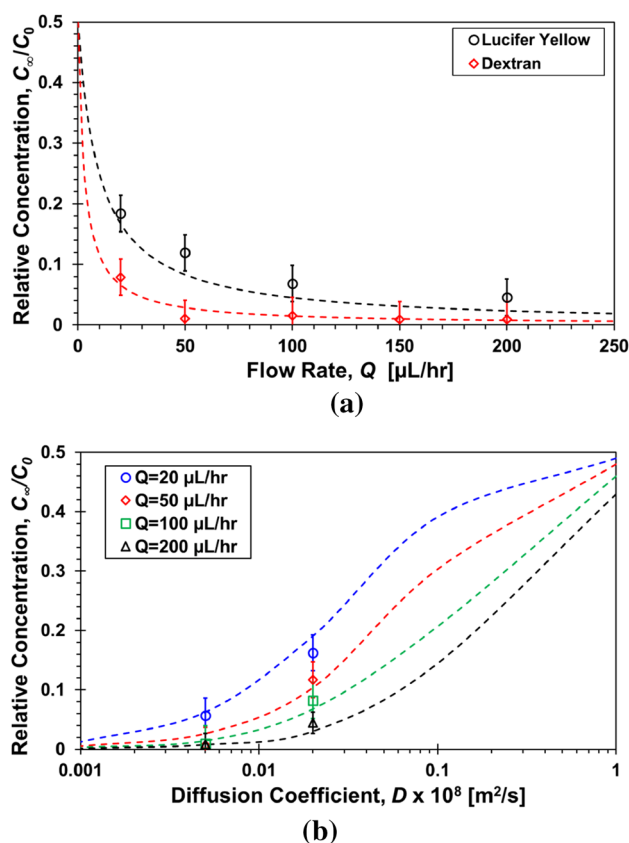

Fig. 8 Relative molecular concentration measurements (symbols) and computations (dash lines) at the bottom channel outlet as a function of: **a** flow rate for Lucifer yellow and dextran, and **b** molecular diffusivity for 20, 50, 100, and 200 μL/h flow rates
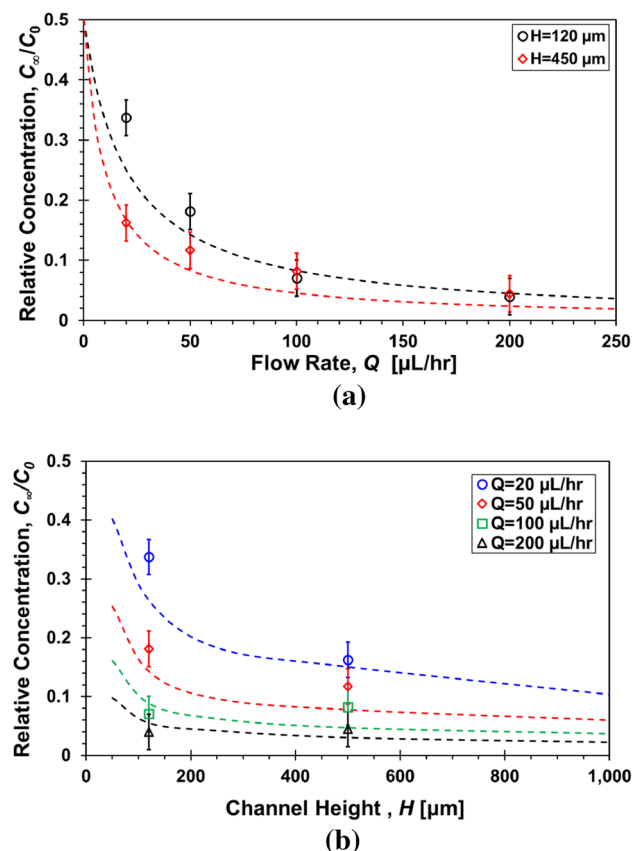

Fig. 9 Relative fluorescein concentration measurements (symbols) and computations (dash lines) at the bottom channel outlet as a function of: **a** flow rate for 120 and 450 μm channel heights, and **b** channel height for 20, 50, 100, and 200 μL/h flow rates with 1% porosity

concentration gradients decrease with increasing channel height reducing the diffusion contribution and the molecular transfer rate. Since these are competing effects, decreasing the channel height by a factor of about four results in a slight increase in the fluorescein steady-state concentration at the bottom channel outlet. The channel height has an appreciable effect at the smaller range, $H < 100$ μm, increasing with decreasing flow rate. For larger channel height range, $H > 100$ μm, the effect is practically undetectable independent of the flow rate.

Finally, the effect of flow direction is investigated. In co-current flows, the concentration gradient across the membrane is the highest at the channel inlets and gradually vanishing towards their outlets. If the channels are long enough, the total molecular transfer is theoretically limited by complete mixing with zero concentration gradient, i.e., $C_\infty/C_0 = 0.5$. However, in counter-current flows, the concentration gradient persists along the entire channels. Hence, depending on the channel length, the bottom channel outlet concentration could exceed this limit with $C_\infty/C_0 > 0.5$. Steady-state fluorescein concentrations at the water channel outlet for both co-current and counter-current flows with 1% porosity are compared in Fig. 10. For the current devices with overlapping channel length of $L = 20$ mm, Fig. 10a, the concentrations for both flow modes are about the same for the entire flow rate range. This suggests that the microchannel length is too short for the manifestation of the flow reversal effect. Indeed, simulation results predict that under the same 20 μL/h flow rate and 1% porosity, Fig. 10b, the outlet fluorescein concentration is higher in counter-current than in co-current flows. The difference between the concentrations of the two flow modes increases with flow rate, and is practically undetectable in short channels, $L < 50$ mm. Furthermore, in the co-current mode, the concentration approaches the limit of $C_\infty/C_0 = 0.5$ asymptotically with increasing channel length. However, in the counter-current mode, the outlet concentration is higher, $C_\infty/C_0 > 0.5$, for very long channels, $L > 150$ mm.

3.3 Simulation profiles

Numerical simulations are particularly valuable for either calculating properties easy to measure but under conditions difficult to realize experimentally or calculating parameters difficult if not impossible to measure even if the conditions can be realized. Using the FLUENT software package, the computed steady-state and time-dependent integrated concentrations were found to agree very well with the experimental measurements confirming the reliability of the numerical results. Indeed, the simulations have been extended to calculate molecular concentrations under conditions not tested in the lab such as high porosity, diffusivity, and microchannel dimensions. Intriguing
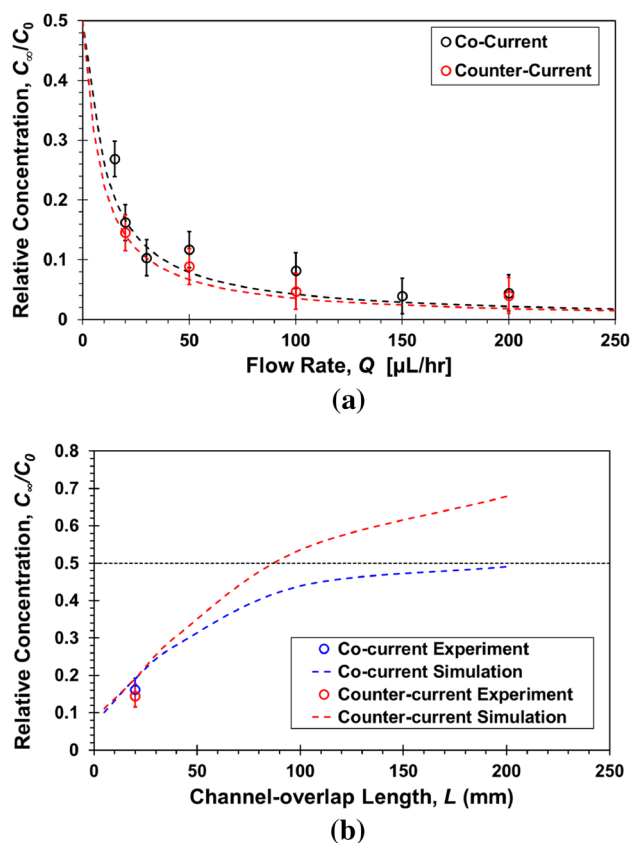

Fig. 10 Relative fluorescein concentration measurements (symbols) and computations (dash lines) at the bottom channel outlet, for co- and counter-current flows, as a function of: **a** flow rate, and **b** channel length under 20 μL/h flow rate with 1% porosity

parameters, extremely difficult to measure experimentally, are the spatial concentration distributions and gradients within the microchannels. An example of the computed steady-state concentration distribution of fluorescein at the central cross-sections of both microchannels, $x = 0$, is demonstrated in Fig. 11 under 20 μL/h flow rate with 1% porosity. Although the cross-section aspect ratio in not large, $W/H \approx 2$, the concentration distribution is fairly two-dimensional, $\partial c/\partial z \approx 0$; hence, the mid-span concentration profile $C(x, y) = c(x, y, z = 0)$ is sufficient to analyze the characteristics of the concentration distributions.

Computed cross-stream concentration profiles are shown in Fig. 12. The streamwise evolution is explored by comparing profiles at three different locations: inlet ($x/L = -1/2$), center ($x/L = 0$) and outlet ($x/L = +1/2$), Fig. 12a, under the same flow rate ($Q = 20$ μL/h). As expected, the inlet profile is almost a step function jumping across the membrane from nearly unity at the top channel to nearly zero at the bottom channel. All profiles feature two distinct regions: (i) near the membrane, diffusion dominates where the concentrations change almost linearly with steep gradients, and (ii) away from the membrane,
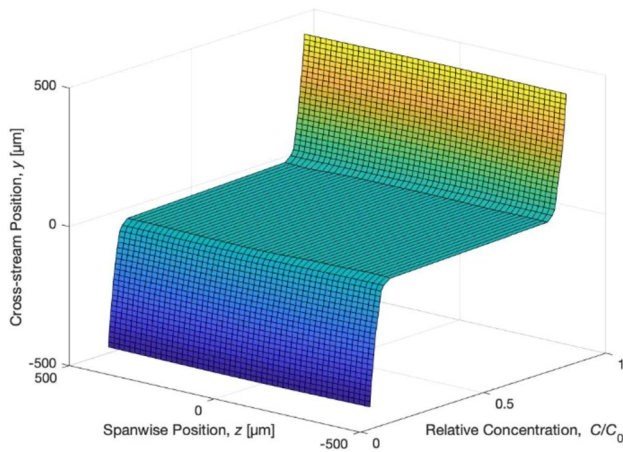
Fig. 11 Computed surface plot of fluorescein spatial concentration distribution at the device central cross-section, $x=0$, for 20 µL/h flow rate with 1% porosity
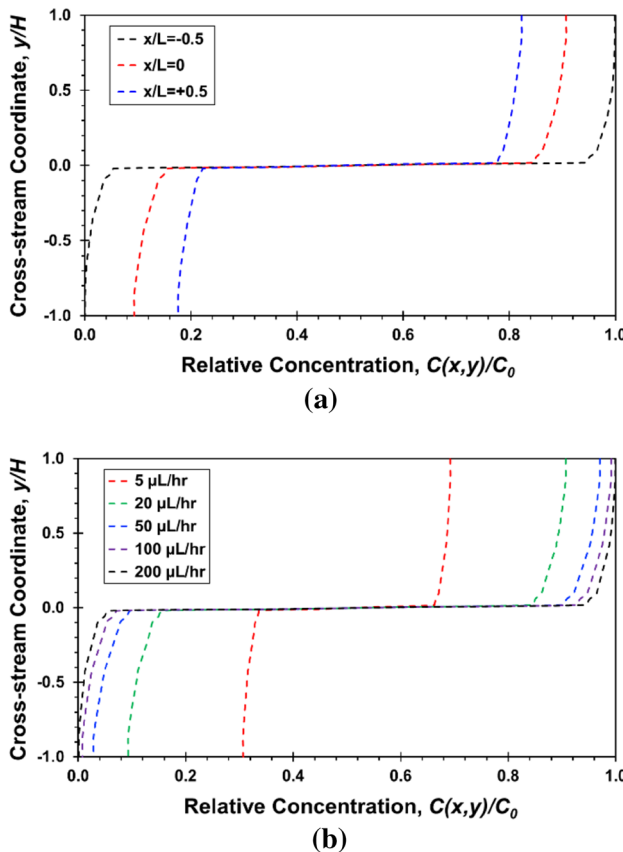

Fig. 12 Computed cross-stream fluorescein concentration profiles: **a** at $x/L = -0.5$, 0, and 0.5 for 20 µL/h flow rate with 1% porosity, and **b** at $x/L = 0$ for 5, 20, 50, 100, and 200 µL/h flow rates with 1% membrane porosity at mid-span ($z=0$)

convection dominates where the concentrations are almost constant with vanishing gradients.

The flow rate effect is demonstrated by comparing profiles at the same location ($x=0$), Fig. 12b, for a wide flow rate range ($Q = 5$–200 µL/h). The concentration gradient decreases with decreasing flow rate approaching a well-mixed system for $Q \rightarrow 0$. As the flow rate increases, the concentration profile approaches a step-like function reducing the mixing level, which could be favorable for long-term maintenance of cell co-cultures.

The length scale dividing the concentration field into the diffusion- and convection-dominant zones emerges as a particularly important feature of the concentration distribution for such applications as organs-on-chips. A promising diffusive layer thickness, δ, can be defined based on the maximum concentration gradient, $(\partial C/\partial y)_{max}$ at $y=0$, to characterize the boundary between these two zones as follows:

$$\delta(x) = \frac{C_T(x) - C_B(x)}{2(\partial C/\partial y)_{max}}. \tag{6}$$

Here, $C_T(x) = C(x, y=H, z=0)$ and $C_B(x) = C(x, y=-H, z=0)$ are the maximum and minimum concentration levels, respectively, at the top and bottom surfaces of the microchannel pair. The streamwise concentration is not constant, $\partial C/\partial x \neq 0$ (Figs. 12a); hence, the concentration distribution field is not strictly fully developed. Furthermore, even for the same central membrane location ($x=0$), the computed concentration profiles vary significantly under different experimental conditions as shown in Fig. 13a. However, the concentration profiles could potentially feature self-similarity characteristics if normalized by local length and concentration scales as follows:

$$\hat{C}(\hat{y}) = \frac{C(x, y) - C_B(x)}{C_T(x) - C_B(x)} \quad \text{and} \quad \hat{y} = \frac{y}{\delta(x)}. \tag{7}$$

Scaled concentration profiles computed for the same experimental conditions have been re-plotted in Fig. 13b. Though not perfect, the reasonable collapse of the normalized concentration profiles onto a single curve suggests that the local scaling is helpful in segregating the two zones. The concentration gradient is almost constant in the diffusion-dominant zone, $\partial \hat{C}/\partial y \approx \text{const}$ at $|\hat{y}| < 1$, with its maximum at the separation membrane. This means that the maximum diffusive mass flux takes place at the interface between the two microchannels supporting the required molecular signaling. The concentration in the convection-dominant zone is almost constant, $\hat{C} \approx \text{const}$ at $|\hat{y}| > 1$, with practically zero gradient. This means that mixing of the fluid flows is limited favoring cultures of different cell types in their respective media. Except for the extreme conditions of very high porosity (10%) and very low flow rate (5 µL/h), the diffuse layer
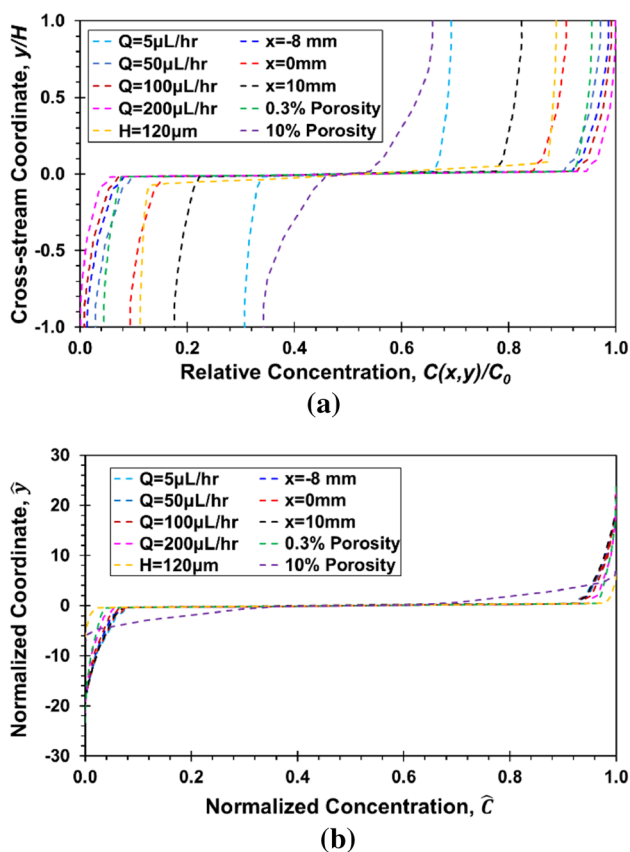
(a)

(b)

Fig. 13 Computed cross-stream fluorescein concentration profiles: **a** for various parameter combinations, and **b** same profiles normalized by local length, $\delta(x)$, and concentration scales, $C_T(x)$ and $C_B(x)$, at mid-span ($z=0$); the solid back curve is a linear fit

Fig. 14 Computed relative concentrations, C_M and C_S, and the cost function, C_F, as a function of the flow rate for a microfluidic bilayer device with 450-μm-high channels, 1% membrane porosity (0.8 μm pore size), and fluorescein as the scalar contaminant

thickness in most profiles is about $\delta \sim 20$ μm, which is on the order of a cell diameter.

Excessive exposure of one cell culture to a harmful component within the other cell culture media could result in cell death. However, a critical feature of the system is the membrane porosity designed to allow communication between the two cell cultures. This cell signaling, enabled by cross-membrane diffusion, is enhanced with decreasing flow rate. Hence, a balancing act may be needed to successfully maintain a co-culture of different cell types requiring both no mixing of incompatible media flows and inter-cellular signaling. An example of a system design to meet this challenge is illustrated in Fig. 14 for a microfluidic device with 450-μm-high channels, 1% membrane porosity (0.8 μm pore size), and fluorescein as the scalar contaminant. The concentration at a cellular layer–fluid flow interface in a device top channel, C_M, is assumed to represent the mixing level experieTTnced by the cells. Similarly, the concentration at the cellular layer–membrane surface interface at the bottom channel, C_S, is assumed to represent the signal level. Both concentrations are computed at the membrane center
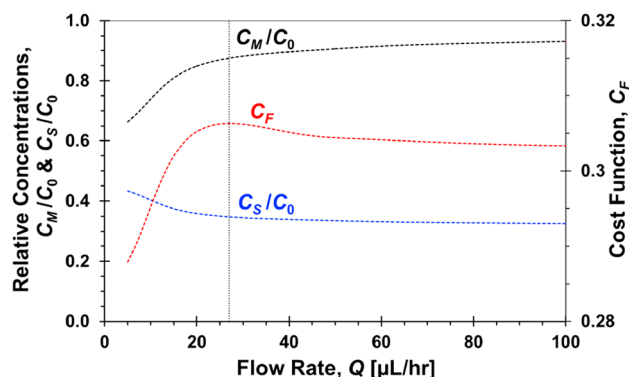
$x=0$ and $z=0$, for various flow rates. Indeed, as the flow rate increases, the concentration at the top channel increases indicating a lower mixing level, while the concentration at the bottom channel decreases indicating a weaker signal level. It is desirable to maximize both concentrations for higher purity media flow in the top channel and stronger cell signaling in the bottom channel. Therefore, a cost function can be defined as a product of the two concentrations: $C_F = (C_M/C_0)(C_S/C_0)$. The maximum value of the cost function at about $Q=27$ μL/h is the optimized flow rate for the design criteria imposed in this example. A different set of design parameters will clearly result in a different optimum flow rate.

4 Conclusion

Experimental and numerical studies of molecular concentration distributions due to convective–diffusive mass transport have been conducted in a microfluidic device designed for organs-on-chips applications. The temporal molecular concentration at the channel outlet, with initial zero concentration, increases almost exponentially with time. The time scale for reaching a steady-state concentration is less than hour, rendering the transient response negligible for culture experiments lasting more than a day. The steady-state concentration is approximately inversely proportional to the flow rate and, similar to the time scale, decreases with increasing flow rate, but changes very little under flow rates higher than 50 μL/h. The steady-state concentration increases almost linearly with increasing porosity, in the range of 0–10%, and levels off with porosity higher than 20%. The effect of molecular size on the concentration distribution is very small for molecules in the range of 1–100 kDa in weight. Under the same flow rate, the

concentration increases with decreasing channel height; however, for channel height larger than the characteristic diffuse layer thickness of 100 μm the height effect is negligible. Reversing the flow direction results in almost the same concentration distribution in short channels but can vary significantly for long channels. Numerically computed spatial distributions reveal an essentially 2D concentration field. A diffuse boundary layer is observed in the cross-stream concentration profiles with local characteristic concentration and length scales. Within the diffuse layer, convection is negligible and the concentration changes almost linearly with distance away from the separation membrane; outside the layer, diffusion is negligible and the concentration is almost constant. This is a key feature enabling long-term culture of cellular layers in their preferred media while allowing cell signaling across the separation membrane. The results shed light on the effects of several control parameters on the resulting molecular concentration distribution and, subsequently, can be used for designing microfluidic devices for applications requiring cell co-cultures such as microphysiological systems.

References

Chung BG, Choo J (2010) Microfluidic gradient platforms for controlling cellular behavior. Electrophoresis 31:3014–3027. https://doi.org/10.1002/elps.201000137

Dichamp J, De Gournay F, Plouraboué F (2017) Theoretical and numerical analysis of counter-flow parallel convective exchangers considering axial diffusion. Int J Heat Mass Transf 107:154–167. https://doi.org/10.1016/j.ijheatmasstransfer.2016.09.019

Edington CD, Chen WLK, Geishecker E et al (2018) Interconnected microphysiological systems for quantitative biology and pharmacology studies. Sci Rep 8:4530. https://doi.org/10.1038/s41598-018-22749-0

Erickson HP (2009) Size and shape of protein molecules at the nanometer level determined by sedimentation, gel filtration, and electron microscopy. Biol Proced Online 11:32–51. https://doi.org/10.1007/s12575-009-9008-x

Esch MB, Sung JH, Yang J et al (2012) On chip porous polymer membranes for integration of gastrointestinal tract epithelium with microfluidic 'body-on-a-chip' devices. Biomed Microdevice 14:895–906. https://doi.org/10.1007/s10544-012-9669-0

Even-Ram S, Yamada KM (2005) Cell migration in 3D matrix. Curr Opin Cell Biol 17:524–532. https://doi.org/10.1016/j.ceb.2005.08.015

Foster KA, Oster CG, Mayer MM et al (1998) Characterization of the A549 cell line as a type II pulmonary epithelial cell model for drug metabolism. Exp Cell Res 243:359–366. https://doi.org/10.1006/excr.1998.4172

Glover K, Strang J, Lubansky A (2014) Characterising the effect of geometry on a microchamber for producing controlled concentration gradients. Chem Eng Sci 117:389–395. https://doi.org/10.1016/j.ces.2014.06.045

Heyman NS, Burt JM (2008) Hindered diffusion through an aqueous pore describes invariant dye selectivity of Cx43 junctions. Biophys J 94:840–854. https://doi.org/10.1529/biophysj.107.115634

Hubatsch I, Ragnarsson EGE, Artursson P (2007) Determination of drug permeability and prediction of drug absorption in Caco-2 monolayers. Nat Protoc 2:2111–2119. https://doi.org/10.1038/nprot.2007.303

Huh D, Matthews BD, Mammoto A et al (2010) Reconstituting organ-level lung functions on a chip. Science (New York, NY) 328:1662–1668. https://doi.org/10.1126/science.1188302

Huh D, Leslie DC, Matthews BD et al (2012) A human disease model of drug toxicity-induced pulmonary edema in a lung-on-a-chip microdevice. Sci Transl Med 4:159ra147. https://doi.org/10.1126/scitranslmed.3004249

Inamdar NK, Griffith LG, Borenstein JT (2011) Transport and shear in a microfluidic membrane bilayer device for cell culture. Biomicrofluidics 5:022213. https://doi.org/10.1063/1.3576925

Jain LNR (1984) Extravascular diffusion in normal and neoplastic tissues. Can Res 44:238–244

Jang K-J, Suh K-Y (2010) A multi-layer microfluidic device for efficient culture and analysis of renal tubular cells. Lab Chip 10:36–42. https://doi.org/10.1039/b907515a

Kim M-C, Lam RHW, Thorsen T, Asada HH (2013) Mathematical analysis of oxygen transfer through polydimethylsiloxane membrane between double layers of cell culture channel and gas chamber in microfluidic oxygenator. Microfluid Nanofluid 15:285–296. https://doi.org/10.1007/s10404-013-1142-8

Kim M, Jia M, Kim Y, Kim T (2014) Rapid and accurate generation of various concentration gradients using polydimethylsiloxane-sealed hydrogel device. Microfluid Nanofluid 16:645–654. https://doi.org/10.1007/s10404-013-1265-y

Kimura H, Sakai Y, Fujii T (2018) Organ/body-on-a-chip based on microfluidic technology for drug discovery. Drug Metab Pharmacokinet 33:43–48. https://doi.org/10.1016/j.dmpk.2017.11.003

Kinsey ST, Locke BR, Dillaman RM (2011) Molecules in motion: influences of diffusion on metabolic structure and function in skeletal muscle. J Exp Biol 214:263–274. https://doi.org/10.1242/jeb.047985

Li Y-J, Cao T, Qin K-R (2018) Transmission of dynamic biochemical signals in the shallow microfluidic channel: nonlinear modulation of the pulsatile flow. Microfluid Nanofluid 22:81. https://doi.org/10.1007/s10404-018-2097-6

Lipowsky H (1995) Shear stress in the circulation. Flow Depend Regul Vasc Funct SE 2:28–45. https://doi.org/10.1007/978-1-4614-7527-9_2

Manneschi C, Pereira RC, Marinaro G et al (2016) A microfluidic platform with permeable walls for the analysis of vascular and extravascular mass transport. Microfluid Nanofluid 20:113. https://doi.org/10.1007/s10404-016-1775-5

Marx U, Walles H, Hoffmann S et al (2012) 'Human-on-a-chip' developments: a translational cutting-edge alternative to systemic safety assessment and efficiency evaluation of substances in laboratory animals and man? Altern Lab Anim 40:235–257

Merchuk JC (1991) Shear effects on suspended cells. Bioreactor systems and effects. Springer, Berlin, pp 65–95

Metallo CM, Vodyanik MA, De Pablo JJ et al (2008) The response of human embryonic stem cell-derived endothelial cells to shear stress. Biotechnol Bioeng 100:830–837. https://doi.org/10.1002/bit.21809

Pisani L (2011) Simple expression for the tortuosity of porous media. Transp Porous Media 88:193–203. https://doi.org/10.1007/s11242-011-9734-9

Ramji R, Roy P (2013) Microfluidic bolus induced gradient generator for live cell signalling. Microfluid Nanofluid 15:99–107. https://doi.org/10.1007/s10404-012-1125-1

Ravetto A, Hoefer IE, den Toonder JMJ, Bouten CVC (2016) A membrane-based microfluidic device for mechano-chemical cell manipulation. Biomed Microdevice 18:31. https://doi.org/10.1007/s10544-016-0040-8

Riahi R, Yang YL, Kim H et al (2014) A microfluidic model for organ-specific extravasation of circulating tumor cells. Biomicrofluidics. https://doi.org/10.1063/1.4868301

Rotenberg MY, Ruvinov E, Armoza A, Cohen S (2012) A multi-shear perfusion bioreactor for investigating shear stress effects in endothelial cell constructs. Lab Chip 12:2696–2703. https://doi.org/10.1039/c2lc40144d

Ruiz A, Joshi P, Mastrangelo R et al (2014) Testing Aβ toxicity on primary CNS cultures using drug-screening microfluidic chips. Lab Chip 14:2860–2866. https://doi.org/10.1039/c4lc00174e

Sakolish CM, Esch MB, Hickman JJ et al (2016) Modeling barrier tissues in vitro: methods, achievements, and challenges. EBioMedicine 5:30–39. https://doi.org/10.1016/j.ebiom.2016.02.023

Salomon JJ, Muchitsch VE, Gausterer JC et al (2014) The cell line NCl-H441 is a useful in vitro model for transport studies of human distal lung epithelial barrier. Mol Pharm 11:995–1006. https://doi.org/10.1021/mp4006535

Sellgren KL, Butala EJ, Gilmour BP et al (2014) A biomimetic multicellular model of the airways using primary human cells. Lab Chip. https://doi.org/10.1039/c4lc00552j

Siyan W, Feng Y, Lichuan Z et al (2009) Application of microfluidic gradient chip in the analysis of lung cancer chemotherapy resistance. J Pharm Biomed Anal 49:806–810. https://doi.org/10.1016/j.jpba.2008.12.021

Song K-Y, Zhang H, Zhang W-J, Teixeira A (2018) Enhancement of the surface free energy of PDMS for reversible and leakage-free bonding of PDMS–PS microfluidic cell-culture systems. Microfluid Nanofluid 22:135. https://doi.org/10.1007/s10404-018-2152-3

Sun J, Liu W, Li Y et al (2017) An on-chip cell culturing and combinatorial drug screening system. Microfluid Nanofluid 21:125. https://doi.org/10.1007/s10404-017-1959-7

Volpatti LR, Yetisen AK (2014) Commercialization of microfluidic devices. Trends Biotechnol 32:347–350. https://doi.org/10.1016/j.tibtech.2014.04.010

Waghmare PR, Mitra SK (2012) A comprehensive theoretical model of capillary transport in rectangular microchannels. Microfluid Nanofluid 12:53–63. https://doi.org/10.1007/s10404-011-0848-8

Wikswo JP, Curtis EL, Eagleton ZE et al (2013) Scaling and systems biology for integrating multiple organs-on-a-chip. Lab Chip 13:3496–3511. https://doi.org/10.1097/MPG.0b013e3181a15ae8.Screening

Winton HL, Wan H, Cannell MB et al (1998) Class specific inhibition of house dust mite proteinases which cleave cell adhesion, induce cell death and which increase the permeability of lung epithelium. Br J Pharmacol 124:1048–1059. https://doi.org/10.1038/sj.bjp.0701905

Zaman MH, Kamm RD, Matsudaira P, Lauffenburger DA (2005) Computational model for cell migration in three-dimensional matrices. Biophys J 89:1389–1397. https://doi.org/10.1529/biophysj.105.060723

Zhang B, Radisic M (2017) Organ-on-A-chip devices advance to market. Lab Chip 17:2395–2420. https://doi.org/10.1039/c6lc01554a